UW-CPTC 09-7

Drift-resistive-inertial ballooning modes in the HSX Stellarator

T. Rafiq[1], C. C. Hegna[2], J. D. Callen[2], and A. H. Kritz[1]

[1]*Department of Physics, Lehigh University, Bethlehem, PA 18015 and*

[2]*Engineering Physics Department,University of Wisconsin, Madison, Wisconsin 53706*

(Dated: August 12, 2009)

Abstract

A linear stability theory of non-ideal magnetohydrodynamic (MHD) ballooning modes is investigated using a two fluid model for electron-ion plasmas. Drift-resistive-inertial ballooning mode (DRIBM) eigenvalues and eigenfunctions are calculated for a variety of equilibria including axisymmetric shifted circular geometry ($\hat{s} - \alpha$ model) as well as for three dimensional configurations relevant for the Helically Symmetric Stellarator (HSX) [F.S.B. Anderson, A.F. Almagri, D.T. Anderson, P.G. Mathews, J.N. Talmadge, and J.L. Shohet, *Fusion Technology* **27**, 273 (1995)]. For typical HSX parameters, characteristic ballooning mode growth rates exceed the electron collision frequency. In this regime, electron inertial effects dominate plasma resistivity and produce an instability whose growth rate scales with the electromagnetic skin depth. However, as plasma β is increased, the resistive and inertial effects become unimportant. Under these conditions, the mode is completely stabilized by drift frequency effects, which dominate resistivity and inertia. Numerical results indicate that in the absence of drift effects, RIBM modes are purely growing and persist in regimes where ideal MHD ballooning modes are stable. It is found that the magnitudes of the linear growth rates are not sensitive to the addition of the mirror term in the description of the HSX stellarator configuration. The eigenvalues and eigenvectors in the strong ballooning approximation are used together with a quasi-linear mixing length estimate to determine particle flux and particle diffusivity. The particle diffusivity increases with rising density gradient and collisionality in a plasma with a low electron temperature. This increase in transport is consistent with the increase observed in the edge region of HSX plasmas. The magnitude of the particle diffusivity is computed to be in the range 5 to 10 m^2/s, which is consistent with the experimental measured particle diffusivity at the edge of HSX plasmas.

I. INTRODUCTION

Unstable resistive ballooning modes (RBMs) may play an important role in producing edge plasma fluctuations and anomalous transport in tokamaks and stellarators. Resistive modes are normally expected to be unstable in the plasma edge region in tokamak discharges. The RBMs grow in the edge region because of the typically low electron temperature and moderately high density. RBMs have been studied in axisymmetric tokamaks using linear [1]-[8] and nonlinear theories [9]-[11]. However, the study of RBMs in fully three-dimensional stellarator geometries is more limited [12]-[16].

Stellarator geometry makes the problem more difficult because of its complicated three-dimensional structure and the related high resolution required in a numerical treatment. In Ref. [14], resistive ballooning modes were studied in general geometry based on the linearized equations of motion of resistive magnetohydrodynamics (RMHD). In that study, a multiple-length-scale expansion technique was used based on a small resistivity and growth rate expansion. RMHD equations computed in Ref. [16] for the Wendelstein 7-X (W7-X) configuration are compared and contrasted to the results with W7-AS using the Correra-Restrepo formulation given in Ref. [14]. In W7-X equilibria, it was shown that the destabilizing effect of resistivity is largely compensated by the stabilizing contribution of plasma compressibility. This behavior persists up to the ideal marginal limit. For W7-AS, where larger resistive effects are observed due to higher resistivity and lower plasma pressure the situation is different. A general theory applicable to 3-D configurations that avoids the usual restrictive assumptions ($\omega \gg \omega_{*en} \gg \omega_\kappa$, where ω is the mode frequency, ω_κ is the curvature drift frequency and ω_{*en} is the electron diamagnetic drift frequency, and zero electron inertia) is not available. It is important to develop a model for the stability limit of RBMs and their dependence on the equilibrium configuration in order to predict the edge transport in both tokamaks and stellarators. This paper is focussed on developing an appropriate model for RBMs.

In this work, a non-ideal MHD ballooning mode model is derived that allows prediction of particle transport in the edge region of the HSX stellartor. In the presence of non-ideal effects, ballooning instabilities can be produced at plasma β levels far below the critical β required for an ideal ballooning instability. Electron inertia, diamagnetic effects, parallel ion dynamics, transverse particle diffusion and perpendicular gyro-viscous stress terms are

included in the calculations. Temperature perturbations, equilibrium temperature gradients and electron trapping are ignored in order to simplify the analysis. For parameters of interest for the Helically Symmetric Experiment (HSX [17]), characteristic growth rates exceed the electron collision frequency. In this regime, electron inertia effects can dominate plasma resistivity and produce an instability whose growth rate scales with the electromagnetic skin depth.

In this paper, a unified theory of RBM and inertial ballooning modes is developed. The theory can be applied to the $k_y \leq 1/\text{cm}$ fluctuations and to the anomalous plasma transport observed in HSX near $r/\bar{a} \simeq 0.7$, where $\bar{a}$ is a minor radius and $T_e \simeq 100eV$. The resistive-inertial ballooning mode eigenvalues and eigenfunctions are numerically evaluated for axisymmetric shifted circular geometry ($\hat{s}-\alpha$ model) as well as 3-D stellarator equilibria.

The organization of this paper is as follows: In Section II, linearized ballooning equations are derived from the Ohm's law, vorticity, continuity and total parallel momentum equations. In Section III, the resistive-inertial MHD (RIMHD), Ideal MHD (IMHD) and drift-resistive-inertial ballooning mode (DRIBM) eigenvalue equations are developed and numerically evaluated for $\hat{s}-\alpha$ geometry. The RIMHD modes in the electrostatic limit are calculated for a 3-D quasihelically symmetric stellarator (QHS) equilibrium. The results for a QHS device are compared and contrasted with those for a magnetic configuration that spoils the helical symmetry by adding mirror terms to the magnetic spectrum [for details, see references [18] and [19]]. In Section IV, the particle diffusivity in the strong ballooning limit is presented by using eigenvalues and eigenvectors together with a quasi-linear estimate. In Section V a discussion of the results and conclusions are presented.

II. Dissipative drift ballooning equations

The reduced Braginskii fluid equations are used for a four-field model of drift resistive ballooning modes with high mode numbers [for details, see references [20] and [21]]. The equations for the parallel component of the generalized Ohm's law, vorticity, electron continuity and total parallel momentum can be written in the following form:

$$E_\parallel + T_e \nabla_\parallel n_e - \eta j_\parallel = \frac{m_e}{e^2 n_e} \frac{\partial j_\parallel}{\partial t}, \tag{1}$$

$$\nabla \cdot n\left(\mathbf{v}_{pi}+\mathbf{v}_{\pi i}\right)+\nabla \cdot n\left(\mathbf{v}_{Di}-\mathbf{v}_{De}\right)+\nabla \cdot\left(n \mathbf{v}_{pe}\right)+\frac{1}{e} \nabla_{\|} j_{\|}=0, \tag{2}$$

$$\frac{\partial n}{\partial t}+\nabla \cdot n\left(\mathbf{v}_{E}+\mathbf{v}_{De}\right)+\nabla \cdot n\left(\mathbf{v}_{pe}+\mathbf{v}_{\eta}\right)+\nabla \cdot\left(n \mathbf{v}_{\| e}\right)=0, \tag{3}$$

$$m_{i} n\left(\frac{\partial}{\partial t}\right) v_{i \|}=-\widehat{\mathbf{b}} \cdot \nabla\left(p_{i}+p_{e}\right)-\widehat{\mathbf{b}} \cdot\left(\nabla \cdot \pi_{i}\right), \tag{4}$$

where

$$E_{\|}=-\nabla_{\|} \phi-\frac{1}{c} \frac{\partial A_{\|}}{\partial t}, \tag{5}$$

$$\mathbf{v}_{E}=-\frac{c}{B} \nabla \phi \times \widehat{\mathbf{b}}, \tag{6}$$

$$\mathbf{v}_{Dj}=-\frac{c}{q_{j} B n} \nabla p_{j} \times \widehat{\mathbf{b}}, \tag{7}$$

$$\mathbf{v}_{\pi i}=-\frac{c}{e B n} \nabla \cdot \pi_{i} \times \widehat{\mathbf{b}}, \tag{8}$$

$$\mathbf{v}_{\eta}=\frac{c}{e B n} \mathbf{R} \times \widehat{\mathbf{b}}, \tag{9}$$

and

$$\mathbf{v}_{pj}=\frac{1}{\omega_{cj}}\left(\frac{\partial}{\partial t}+\mathbf{v}_{j} \cdot \nabla\right) \mathbf{v}_{j} \times \widehat{\mathbf{b}}. \tag{10}$$

Here $\widehat{\mathbf{b}}=\mathbf{B}/|B|$ is the unit vector along the magnetic field line, $\omega_{ci}=eB_0/m_ic$ is the ion cyclotron frequency evaluated at the magnetic axis, $\mathbf{j}_{\|}=en(v_{\|i}-v_{\|e})$ is the plasma current parallel to the magnetic field, ϕ is the electrostatic potential, $p=n(T_i+T_e)$ is the isotropic pressure, T_j is the equilibrium temperature of species j (which is assumed to be constant), and π_i is the anisotropic ion stress tensor. The velocity $\mathbf{v}_{\pi i}$ is due to the stress tensor π, which contains a viscosity part and a finite Larmor radius part, (cf. p.20 in reference [4]) and $\mathbf{R}$ denotes the frictional force. The electron stress tensor is neglected and electron and ion densities are both denoted by n. To the lowest order ($\omega \ll \omega_{ci}$), $\mathbf{v}_j = \mathbf{v}_E + \mathbf{v}_{Dj}$ is substituted into the above polarization flow $\mathbf{v}_{pj}$ for species j. However, the total ion and electron velocities used in the Eqs. (2) and (3) are

$$\mathbf{v}_{i}=\mathbf{v}_{E}+\mathbf{v}_{Di}+\mathbf{v}_{pi}+\mathbf{v}_{\pi i}+\mathbf{v}_{\| i}, \tag{11}$$

$$\mathbf{v}_{e}=\mathbf{v}_{E}+\mathbf{v}_{De}+\mathbf{v}_{pe}+\mathbf{v}_{\eta}+\mathbf{v}_{\| e}. \tag{12}$$

Note that the perpendicular electric field in Eq. (6) is electrostatic in the limit of low β. Electromagnetic effects, other than Ohm's law, are included in these model equations through the parallel gradient $\nabla_{\|}=\widehat{\mathbf{b}} \cdot \nabla=\widehat{\mathbf{b}}^{(0)} \cdot \nabla+\widehat{\mathbf{b}}^{(1)} \cdot \nabla$ where $\widehat{\mathbf{b}}^{(0)}$ is the direction of the unperturbed magnetic field, and $\widehat{\mathbf{b}}^{(1)}=\nabla \times \widetilde{\mathbf{A}}_{\|}/B=\nabla \widetilde{\mathbf{A}}_{\|} \times \widehat{e}_{\|}/B$ is the magnetic

perturbation associated with field line bending, $A_\parallel$. It follows that, when $\widehat{\mathbf{b}}^{(1)}\cdot\nabla$, operates on variable the equilibrium S_0, it has the linearized form, -$iS_0\omega_{*S}\widehat{A}_\parallel$, where $\omega_{*s}=-\left(cT_e/eB\right)\mathbf{k}\cdot\widehat{e}_\parallel\times\nabla\ln S_0$.

When quasi-neutrality is assumed, $n=n_e=n_i$, Ampére's law reduces to

$$\nabla_\perp^2\widetilde{A}_\parallel=-\frac{4\pi}{c}\widetilde{j}_\parallel \tag{13}$$

Equations (1)-(4) can be written, using $\nabla_\perp=ik_\perp$, $\partial/\partial t=-i\omega t$, in the following linearized form in $\omega\sim\omega_s\sim\omega_{*j}\sim\omega_\eta$ maximal ordering

$$\left(\omega-\omega_{*en}+\omega H+ic^2k_\perp^2\eta_\parallel/4\pi\right)\widehat{\Psi}=-ic_s\nabla_\parallel^{(0)}\left(\widehat{\Phi}-\widehat{n}\right), \tag{14}$$

$$\omega k_\perp^2\rho_i^2\left(\widehat{n}+\tau\widehat{\Phi}\right)=\omega_\kappa\widehat{n}+k_\perp^2\rho_e^2\left(\omega-\omega_{*en}\right)\widehat{\Phi}-i\mu_\perp k_\perp^4\rho_i^2\left(\widehat{n}+\tau\widehat{\Phi}\right)-i\frac{\tau v_A^2}{c_s}\nabla_\parallel^{(0)}\left(k_\perp^2\rho_i^2\widehat{\Psi}\right), \tag{15}$$

$$\omega\widehat{n}-\omega_{*en}\widehat{\Phi}=\omega_{\kappa e}\left(\widehat{\Phi}-\widehat{n}\right)+k_\perp^2\rho_e^2\left(\omega-\omega_{*en}\right)\widehat{\Phi}-ic_s\nabla_\parallel^{(0)}\widehat{\mathbf{v}}_\parallel+i\frac{\eta_\perp c^2k_\perp^2}{4\pi}\frac{c_s^2}{v_A^2}\widehat{n}+i\frac{\tau v_A^2}{c_s}\nabla_\parallel^{(0)}\left(k_\perp^2\rho_i^2\widehat{\Psi}\right), \tag{16}$$

$$\left(\omega+\omega_{\kappa i}\right)\widehat{\mathbf{v}}_\parallel+\omega_{*en}\widehat{\Psi}=-ic_s\nabla_\parallel^{(0)}\widehat{n}-4i\mu_\perp k_\perp^2\widehat{v}_\parallel. \tag{17}$$

Here, $H\equiv k_\perp^2\delta_e^2$, $\delta_e^2\equiv c^2/\omega_{pe}^2$ is the electromagnetic skin depth, c is the speed of light, ω is the mode frequency, $\omega_{pe}^2\equiv4\pi ne^2/m_e$ is the electron plasma frequency, e is the electron charge, m_j is the mass of species j, $\mu_\perp\equiv0.3\nu_{ii}\rho_i^2$ is the classical perpendicular viscosity, $\rho_i\equiv v_{ti}/\omega_{ci}$ is the ion Larmor radius, $\nu_{ii}=(4/3)(\sqrt{\pi}ne^4\lambda)/\sqrt{m_i}T_i^{3/2})$, λ is the Coulomb logarithm, $v_{ti}\equiv\sqrt{T_i/m_i}$ is the ion thermal velocity, $\omega_{ci}\equiv eB/m_ic$ is the ion cyclotron frequency, m_i is the ion mass, $\tau\equiv T_e/T_i$ is the ratio of electron to ion temperature, $\rho_e\equiv v_{te}/\omega_{ce}$ is the electron Larmor radius, $v_A^2\equiv B^2/4\pi nm_i$ is the Alfvén speed, and $\eta_\parallel$ and $\eta_\perp$ are the longitudinal and transverse Spitzer resistivities. Here, $\widehat{\Psi}\equiv ec_s\widetilde{A_\parallel}/cT_e$, $\widehat{\Phi}\equiv e\widetilde{\phi}/T_e$, $\widehat{v}_\parallel\equiv\widetilde{v_{\parallel i}}/c_s$, and $\widehat{n}\equiv\widetilde{n}/n$, are the dimensionless perturbed parallel component of vector potential, electrostatic potential, parallel ion flow and density, respectively. The frequency ω_{*en} in Eq. (14) is the diamagnetic drift frequency $[\omega_{*en}=-\left(cT_e/eB\right)\mathbf{k}\cdot\widehat{e}_\parallel\times\nabla\ln n]$, and the frequency ω_κ in Eq. (15) is the curvature drift frequency ($\omega_\kappa\equiv\omega_{\kappa i}+\omega_{\kappa e}$) in which $\omega_{\kappa j}\equiv(2cT_j/eB)\,\mathbf{k}\cdot\widehat{e}_\parallel\times\kappa$, where $\kappa=(\widehat{\mathbf{e}}_\parallel\cdot\nabla)\widehat{\mathbf{e}}_\parallel$ is the curvature vector and $c_s\equiv\left(T_e+T_i/m_i\right)^{1/2}$ is the sound speed.

III. Ballooning equations in shifted circular geometry

Before considering detailed calculations of quasi-helically symmetric stellarators, we carry out the stability properties of a shifted circular geometry. While the geometry of this section is not a good representation for HSX plasmas, we use these calculations to compare with the stellarator specific work of the next section.

Ballooning modes are pressure-driven instabilities for modes with finite $k_\parallel$. For the interchange perturbation, the parallel component of the propagation vector is zero ($k_\parallel = 0$), and an average minimum-B condition is stabilizing to the instability. When studying a perturbation in which $k_\parallel \neq 0$ but $k_\parallel/k_\perp \ll 1$, instabilities can be produced that are localized in the bad curvature region. This type of instability is called a ballooning instability. Ballooning instabilities can be resistive or ideal depending upon whether the electron motion parallel to the field is impeded as a result of collisions or inductive fields. For HSX like parameters [17], the characteristic growth rate exceeds the electron collision frequency. Therefore, the electron inertia is included in the parallel Ohm's law. In this Section, eigenvalue equations are derived, after employing the standard high n ballooning mode formalism [22], for drift-resistive-inertial ballooning (DRIBM), resistive-inertial MHD (RIMHD) and ideal MHD (IMHD) modes.

The DRIBM equation can be written as follows after ignoring parallel ion momentum, perpendicular viscous stress, and the transverse particle diffusion terms and by using $\nabla_\parallel^{(0)} = (1/qR)d/d\theta$ in Eqs (14)-(17):

$$\omega_A^2 \frac{d}{d\theta}\left(\frac{k_\perp^2\rho_s^2}{\omega_{Pe}+\omega_R\widehat{k}_\perp^2}\frac{dU}{d\theta}\right) = \frac{\omega_k\left(\omega_{ke}-\omega_{*en}\right)+\left(\omega_k-\omega+\omega_{ki}\right)\omega_{Pi}k_\perp^2\rho_s^2}{\omega_{Pe}+\left(1+1/\tau\right)\omega_{ke}+\omega_{Pi}k_\perp^2\rho_s^2}U. \tag{18}$$

The quantity $U = \Phi - \widehat{n}$ is the non-adiabatic response; $\omega_A = v_A/qR$ is the Alfvén frequency where q is the safety factor and R is the major radius; $k_\perp = k_\theta\widehat{k}_\perp\left(\theta\right)$ where $k_\theta = (n_\phi q/r)$ is the poloidal wave vector, n_ϕ is the toroidal mode number, and $\widehat{k}_\perp^2\left(\theta\right) = 1+\left(\hat{s}\theta-\alpha\sin\theta\right)^2$; $\alpha = 2q^2\beta/\epsilon_n$ is the ballooning parameter, and $\hat{s} = \left(d\ln q/d\ln r\right)$ is the magnetic shear; $\omega_{Pj} = \omega - \omega_{*jn}$; $\rho_s \equiv c_s/\omega_{ci}$ is the ion larmor radius, $\beta \equiv 8\pi n(T_e+T_i)/B^2$; $\omega_{\kappa e}/\omega_{*en} = \epsilon_n g\left(\theta\right)$, with $g\left(\theta\right) = [\cos\theta+(\hat{s}\theta-\alpha\sin\theta)\sin\theta]$, $\epsilon_n = L_n/R$, $L_n = \left(-d_r\ln n\right)^{-1}$; and $\omega_R = \omega\delta_e^2k_\theta^2+i\omega_\eta$ where $\omega_\eta = \left(c^2\eta_\parallel/4\pi\right)\left(n_\phi q/r\right)^2$ is the resistive frequency.

The resistive-inertial MHD incompressible ballooning equation (RIMHD) in the high

frequency ($|\omega| \gg \omega_{*en}, \omega_{ke}$), long wavelength ($k_\theta^2 \rho_i^2 \ll 1$) limit can be written as follows:

$$\omega_A^2 \frac{d}{d\theta}\left(\frac{\widehat{k}_\perp^2}{\omega + (\omega c^2 k_\theta^2/\omega_{pe}^2 + i\omega_\eta)\widehat{k}_\perp^2}\frac{d\widehat{\Phi}}{d\theta}\right) + \omega \widehat{k}_\perp^2 \widehat{\Phi} + \frac{\omega_{\kappa e}\omega_{*en}}{\omega k_\theta^2 \rho_s^2}\left(1+\frac{1}{\tau}\right)\widehat{\Phi} = 0. \qquad (19)$$

Note that the electron inertia term, $\omega c^2 k_\theta^2/\omega_{pe}^2$, is present in Eqs. (18) and (19). The standard incompressible ideal MHD (IMHD) ballooning equation can be recovered by neglecting electron inertia and resistivity in the RIMHD equation, Eq. (19),

$$\omega_A^2 \frac{d}{d\theta}\left(\widehat{k}_\perp^2 \frac{d\phi}{d\theta}\right) + \omega^2 \widehat{k}_\perp^2 \phi + \frac{\omega_{\kappa e}\omega_{*in}}{k_\theta^2 \rho_i^2}\left(1+\frac{1}{\tau}\right)\phi = 0, \qquad (20)$$

where the usual finite Larmor-radius-effect (FLR) (for $k_\perp \rho_i \ll 1$) can be included by substituting $\omega\,(\omega - \omega_{*in})$ for ω^2 in Eq. (20).

IIIa. Results in shifted-circular geometry

Equations (18)-(20) are solved numerically by using a standard root finding algorithm for axisymmetric shifted-circle equilibria, which are the equilibria used in obtaining the results shown in Figs. 1-6. For all cases, the parameters used are those appropriate for HSX edge plasmas ($r/\bar{a} \sim> 0.7$): $T_e = 100\mathrm{eV}$, $T_i = 25\mathrm{eV}$, $B \simeq 0.5\mathrm{T}$, $n_e \simeq 10^{18}\mathrm{m}^{-3}$, $q = 1.0$, $\hat{s} = -0.03$, and $\beta = 2 \times 10^{-4}$.

The right panel in Figure 1a shows the normalized growth rate (γ/ω_A) of the IMHD, RIMHD and ideal MHD modes with electron inertia (RIMHD in the limit of $\eta = 0$) as a function of the normalized pressure gradient (the ballooning parameter α), for $\theta_k = 0$, $\hat{s} = 0.1$, $k_\theta \rho_s = 0.3$, $\hat{\nu} = \nu_{ei}/\omega_A = 0.023$, and $\beta = 0.0002$. In this scan, a positive global magnetic shear, $\hat{s} = 0.1$, is chosen to illustrate the ideal MHD unstable region. HSX has reverse shear in the tokamak sense (negative value of $\hat{s}$). However, the magnetic geometry of the shifted circle is completely inappropriate to model HSX plasmas. In the presence of 3-D shaping, ideal MHD ballooning instabilities can be excited when $\hat{s} < 0$ [23].

The electron inertia and resistivity result in an instability when the ideal MHD mode is stable. The electron inertia and resistive modes are purely growing ($\omega_r = 0$). For HSX-relevant parameters, the electron inertia modes (the RIMHD case for $\eta = 0$) are found to be more important than the resistive modes due to the existence of RIMHD modes in the first ideal stability region. Note that RIMHD modes persist in the ideal MHD second stable regime. Both the electron inertia and resistive instabilities are characterized by broad

eigenfunctions along the field lines as shown in Figs. 1a and 1b. The eigenfunctions are found to be relatively strongly localized along the field line at higher values of the ballooning parameter α, as shown in the right panel of Fig. 1b. Moreover, the qualitative nature of the eigenfunctions is insensitive as to whether or not electron inertia is present. The electron inertia and resistive ballooning eigenfunctions are found to be broad for HSX-relevant values of the ballooning parameter ($\alpha \ll 1$). Therefore, the assumptions $|\omega| \gg \omega_{*en} \gg \omega_{ke}$ and $k_\theta^2 \rho_i^2 \ll 1$ needed for MHD applicability become suspect and, for a more satisfactory stability analysis, a two fluid formulation is required.

Figure 2 shows the eigenvalues obtained for the drift-resistive-inertial ballooning mode (DRIBM) derived using Eq. (18) in which diamagnetic and first order FLR effects are included. The growth rates of DRIBM are compared with the growth rates of RIMHD modes using the same parameter values as used in Fig. 1, except choosing stellarator-like global shear $\hat{s} = -0.03$ and $k_\theta \rho_s = 0.1$. The FLR and diamagnetic effects are found to be slightly stabilizing for RIMHD modes that propagate in the electron diamagnetic flow direction. These stabilizing effects increase the critical α in the first stability region. The RIMHD modes are purely growing (zero real frequency). The real frequency of the DRIBM mode is shown in the right panel in Fig. 2a where negative values of ω_r indicate mode frequencies in the ion diamagnetic direction. All of these modes are still characterized by broad eigenfunctions in ballooning space. This indicates a strong radial localization in configuration space. As shown in Fig. 2b, the width in ballooning space decreases as the ballooning parameter α increases.

In Fig. 3a, the variation of the normalized growth rate and the real frequency are shown as a function of global magnetic shear $\hat{s}$ with $\alpha = 0.1$. The other parameters are the same as in Fig. 2. A reversed magnetic shear is found to be more stabilizing than positive magnetic shear because the normal and geodesic curvature in the $g(\theta) = [\cos\theta + (\hat{s}\theta - \alpha \sin\theta)\sin\theta]$ function counteract each other and reduce the destabilizing toroidal effects [4]. We reiterate that the geometry of the shifted circle is inappropriate for direct HSX comparison. Nonetheless, some inferences from these calculations can be made. The effects of reversed magnetic shear not only reduce the growth rate but, also, extend the eigenfunction along the ballooning angle, as shown in Fig. 3b. The q-profile in HSX has a nearly flat q-profile, a low local magnetic shear and an unfavorable magnetic curvature at the $\theta_0 = 0 = \zeta_0$ point of the magnetic surface, where θ_0 and ζ_0 are the extended poloidal and toroidal angle like coordinates. Therefore,

DRIBM modes will be unstable in a device with the HSX geometry because these types of modes have large amplitude (balloon) in the region of bad local curvature (for the instability drive) and low local magnetic field shear (to minimize stabilizing effect of field line bending) within each field period. The unstable modes have an envelope that extends over many field periods along field lines. Hence, the modes are highly localized radially.

The growth rate is plotted in Fig. 4 as a function of $k_\theta \rho_s$ with $\hat{s} = -0.03$ for the RIMHD and DRIBM instabilities. The other parameters are the same as used to obtain the results shown in Fig. 2. All parts of the k-spectrum are found to be unstable in the incompressible RIMHD mode. However, for the DRIBM instability, the diamagnetic and FLR effects reduce the growth rate and completely stabilize the mode for $k_\theta \rho_s \geq 0.2$. Even for $k_\theta \rho_s \to 0$, the growth rate of the DRIBM instability is found to be smaller than the growth rate of the RIMHD instability, which indicates the stabilizing effects of the secularity of the magnetic drift frequency. The real frequency of the DRIBM mode is found to decrease with increasing $k_\theta \rho_s$. Generally, two fluid effects are found to be stabilizing for the RIMHD mode. Note that the ion temperature gradient, the parallel ion dynamics and $\mathbf{E}\times\mathbf{B}$ flow shear are not included in these numerical results. These effects can all decrease the growth rate of the DRIBM further. For the chosen plasma parameter values, the inclusion of temperature gradient can lead to FLR stabilization for values of $k_\theta \rho_s$ smaller than 0.2. However, for flow shear stabilization, one would apparently need $\gamma < \omega_E \simeq 30 E_r$, or $E_r = 100\text{V/cm}$. Additionally, since $T_i << T_e$ in HSX plasmas, one would not expect ion temperature gradient effects to play an important role.

The dependence of γ and ω on the density scale length $\epsilon_n = L_n/R$ where $L_n = (d_r \ln n)^{-1}$ is shown in Fig. 5 for $q = 1.0$, $\hat{s} = -0.03$, $\alpha = 2q^2\beta/\epsilon_n$, $\tau = 1.0$, $\beta = 0.002$, $k_\theta \rho_s = 0.1$ and $\theta_k = 0$. It is found that as ϵ_n increases, the growth rate decreases, while the real frequency also decreases in magnitude. The mode is completely stabilized for $\epsilon_n \leq 0.02$ and for $\epsilon_n \geq 0.112$. For small ϵ_n, the mode is stable since $|\omega_\kappa|/\omega \ll 1$ and for $\epsilon_n \geq 0.112$, the mode vanishes due to compressibility effects. At low density gradients, growth rates decrease and the eigenfunction becomes broader along the field line as shown in Fig. 5b.

The variation of the growth rate and real frequency is shown in Fig. 6 as a function of β for $k_\theta \rho_s = 0.01$, and $\tau = 0.025$, where the other parameters are the same as those used to obtain the results shown in Fig. 5. There is no mode threshold at low values of β, even for $\beta = 0.01$. However, as β increases above .05, the growth rate and real frequency decrease

and the mode becomes completely stabilized at $\beta = 0.17$. This is due to ω_* stabilization at high β. As shown in Fig. 6b, the resistive and inertia effects become unimportant for $\beta \sim 0.17$, and the transition to an ideal mode results under these conditions.

In order to illustrate the DRIBM mode threshold as a function of β, the growth rate and real frequency are plotted in Fig. 7a as a function of β for $k_\theta \rho_s = 0.2$, and $\tau = 4.0$, where the other parameters are the same as employed in Fig 6. For $k_\theta \rho_s = 0.2$, and for higher electron temperature plasmas, the stability threshold is found at $\beta \approx 0.006$. The ballooning mode eigenfunction is shown in Fig. 7b as a function θ for $\beta = 0.006$ and $\beta = 0.012$.

IIIb. Results for a plasma with HSX geometry

Equation (19) is solved numerically in the electrostatic limit using three dimensional equilibria for a quasi-helically symmetric (QHS) stellarator and a configuration whose ("Mirror") symmetry is spoiled by the presence of magnetic mirror contribution to the magnetic spectrum [17]. The ballooning mode formalism and WKB type boundary conditions [24, 25] are used to solve an eigenvalue problem for the resistive-inertial MHD equation in the electrostatic limit using a fully three-dimensional hydrodynamic equilibria. The equilibria are computed using the VMEC code [26] with fixed boundary conditions for QHS and Mirror mode configurations and for a set of 98 magnetic surfaces. The VMEC coordinate system is not a straight field line coordinate system. Thus, before the resistive-inertial MHD ballooning equation is solved in the electrostatic limit, the equilibria is first transformed to Boozer coordinates [27]. Then, the contravariant and covariant basis vectors are constructed for each flux surface and used to calculate the magnetic field, the magnetic field line curvature, the local magnetic shear, and the derivatives of the magnetic field in a fully three dimensional configuration. The details are described in Ref. [28].

Figure 8 contains a plot of the growth rate γ, normalized by ω_A, as a function of $(k_\perp \rho)^2$ (evaluated at $\zeta = \zeta_0$) for $\tau = 1$, $R\nu_{ei}/2c_s = 0.42$, $\theta_k = 0.0$, and $\epsilon_n = 0.07$. This calculation is carried out for the field line that intersects the location $\theta_0 = 0$, $\zeta_0 = 0$ on the normalized magnetic surface $s = 0.8980$ as given in [29]. This point is chosen because it is thought to be the most unstable since the local magnetic shear is small, the local value of the geodesic curvature is zero and the destabilizing influence of the normal curvature is strongest. In the left panel of Fig. 8, the bottom curve, denoted with squares, is for the highly resistive case

(HR) where $\delta_e = 0$, $\nu_e \neq 0$; the middle curve, denoted with x's, is for the collisionless case ($\nu_e = 0$, $\delta_e \neq 0$); and the top curve, denoted with diamonds, is for nonzero electron inertia and collisionality (EI+collisions). All three cases are found to be unstable for QHS relevant parameters, and, in each case, the growth rate increases with increasing mode number. The corresponding mode structures are shown in the right panel of Fig. 8 for $(k_\perp \rho)^2 = 0.24$. In comparison with the ion temperature gradient and drift modes calculated in electrostatic limit in our earlier published work [19, 28], these modes are found to be very extended ($\zeta_0 = 20\pi$) along the magnetic field line. However, as the growth rate increases for each of the cases, the eigenfunctions become relatively localized.

The highly resistive (HR: $\delta_e = 0$, $\nu_e \neq 0$) growth rate in QHS, compared with the growth rate for the corresponding Mirror case is illustrated in Fig. 9. In both configurations, the magnitudes of the linear growth rates are found to be comparable, indicating roughly the same level of anomalous transport flux that is observed in the edge region of experiments [30]. This result is consistent with our earlier findings for ITG and drift modes [19, 28]. The common stability properties are due to the similar structure of the curvature and the local magnetic shear.

Although the shifted circular geometry is very different than the QHS and mirror geometries. The magnitude of the growth rates in all three geometries are found to be comparable and the eigenfunctions, in all cases, are extended along the magnetic field lines and have similar structure. The periodicity in the eigenfunctions is, however, found to be different in the shifted circular geometry and the HSX geometries.

IV. The particle diffusivity in the strong ballooning limit

HSX is a low magnetic shear stellarator. In a plasma with low shear, the RBM modes are expected to be extended along the magnetic field lines. This is shown in Section IIIa and Section IIIb by computing eigenfunctions of RBMs in various limits as a function of ballooning angle θ. In the previous sections, second order differential eigenvalue equations are solved numerically in different limits by using a standard shooting technique. In this section the full RBM model (Eqs. 14-17) is solved to estimate the effective particle diffusivity (D_n) in a strong ballooning limit. The algebraic method is used to calculate eigenvalues and eigenvectors. The effective particle diffusivity is computed directly from the eigenvalues and

the eigenvectors.

The flux of particles produced by the perturbed $\mathbf{E}\times\mathbf{B}$ motion of the plasma is

$$\Gamma = \tilde{n}\tilde{v}_E^* + c.c. = 2(\mathrm{Re}\tilde{n}\,\mathrm{Im}\tilde{\phi} - \mathrm{Im}\tilde{n}\,\mathrm{Re}\tilde{\phi})k_y/B. \tag{21}$$

The saturation level of the turbulence is computed using the quasilinear approximation

$$\frac{e\tilde{\phi}}{T_e} \approx \frac{1}{k_x\rho_s}\frac{\gamma}{k_y c_s} = \frac{2}{Rk_x}\frac{\gamma}{\omega_{\kappa e}}, \tag{22}$$

which is used to compute the particle flux given by

$$\frac{\Gamma}{n}\frac{Rk_x^2}{\omega_{\kappa e}} = 2\hat{\gamma}^2(\mathrm{Re}\hat{n}\,\mathrm{Im}\hat{\Phi} - \mathrm{Im}\hat{n}\,\mathrm{Re}\hat{\Phi})/|\hat{\Phi}|^2, \tag{23}$$

where $\hat{\gamma} = \gamma/\omega_{\kappa e}$ is the growth rate normalized to the electron magnetic drift frequency.

In order to estimate particle diffusivity due to DRIBM in the HSX stellarator the following values are considered: $n = 10^{18}\,\mathrm{m}^{-3}$, $\mu_\perp = 0.0$, $B = 0.5\,\mathrm{T}$, $\bar{a} = 0.12\,\mathrm{m}$, $\bar{R} = 1.2\,\mathrm{m}$, $q = 1.0$, $\hat{s} = 0.03$, $Z_{eff} = 1.5$, $\nabla \mathrm{T}_i = 0.0$ and $k_\perp\rho_s = 0.1$. The value of $k_\perp\rho_s = 0.1$ is chosen because at this wavelength the growth rate is found (using the shooting method, see Fig. 4) to be maximum for the DIRBM mode. The expression for parallel wavenumber $k_\parallel = \sqrt{\alpha}/(qR)$ is used, which is estimated in Ref. [31] in terms of the ballooning parameter α by

$$\alpha = \left(k_1 + \sqrt{k_1 + \hat{s}^2 k_2}\right)/2, \tag{24}$$

with

$$k_1 = \frac{q^2}{4}\left(k_\perp\rho\right)^2\sqrt{\frac{T_i}{T_e}\frac{(g_{Ti}+g_n)}{2(1-f_t)}}, \qquad k_2 = q^2\left(k_\perp\rho\right)^4\frac{T_i}{T_e}\frac{(g_{Ti}+g_n)}{2(1-f_t)}, \qquad f_t \approx \sqrt{\frac{2\epsilon_H}{1+\epsilon_H}}, \tag{25}$$

where f_t is the trapped electron fraction, $\epsilon_H = 1.4\ r/R$ is the helical ripple in HSX, g_{Ti} and g_n are the normalized ion temperature and density gradients [$g_{ji} \equiv 1/\epsilon_j$, $\epsilon_j = L_j/R$, $L_j = (-d_r \ln j)^{-1}$].

Fig 10 shows the effective particle diffusivity D_n due to a full DRIBM model (the solid curve) plotted against the normalized density gradient, $g_{ni} = -R\hat{x}\cdot\nabla n/n = 1/\epsilon_n$. The effect of omitting electron inertia is indicated by the curve denoted with squares and the effect of omitting parallel ion dynamics are indicated by the dashed curve are also illustrated. It is seen that D_n increases with density gradients. The magnitude of the particle diffusivity is in the range (5-10 m^2/s), which is comparable to the experimental measured particle diffusivity

at the edge of HSX plasmas. The stabilizing effects of parallel ion dynamics ($v_\parallel \neq 0$) are found to be very small due to the small ion temperature. Electron inertia effects are found to have an effect only for large density gradients. Note that these results are presented in the limit of strong ballooning, where electron inertia is not expected to play a dominant role due to a strong localization of the eigenfunctions.

Fig 11 shows the effective particle diffusivity plotted against the normalized density gradient, for electron temperature T_e as a parameter. In this scan electron temperature $Te = 10\,\text{eV}$, $20\,\text{eV}$, $30\,\text{eV}$ and $40\,\text{eV}$ are considered while the ion temperature $T_i = 10\,\text{eV}$ is assumed. The selected values of electron and ion temperatures are appropriate for the edge region of HSX plasmas. It is observed that the particle diffusivity D_n increases with decreasing electron temperature.

The particle diffusivity D_n dependence on electron ion collision frequency (ν_{ei}) is shown in Fig. 12 with $g_n = 10$, and $\tau = T_e/T_i = 2.0$. All other HSX parameters are the same as those used in Fig. 10. It is found that as electron collision frequency increases, the particle transport increases as well. In summary, the increase at low electron temperature seen in particle diffusivity with density gradient and collisionality indicates that the DRIBM model predicts an increase in transport with radius as observed in edge region of the HSX stellarator.

V. Conclusions

A unified theory that includes both resistive and electron inertial ballooning modes has been developed. The drift-resistive-inertial ballooning mode (DRIBM) is characterized by eigenfunctions that are extended along the field line in ballooning space. The qualitative nature of the eigenfunctions is found to be insensitive to whether or not electron inertia is present. However, the resistive and inertial effects become unimportant as the plasma β is increased close to the transition to an ideal MHD mode. In the absence of two fluids drifts effects, the modes are purely growing and they persist in regimes where ideal MHD ballooning modes are stable. For parameters of interest to HSX, electron inertia effects are more important than plasma resistivity. The magnitude of the linear growth rates is not sensitive to the magnetic configuration in HSX plasmas. This result would indicate a comparable level of anomalous transport in QHS and mirror configurations and is consistent

with experimental observations in the edge region of the HSX stellarator [30]. The common stability properties in the QHS and mirror configurations in the HSX are due to the similar structure of the curvature and local magnetic shear. The increase in particle diffusivity with increasing density gradient and collisionality at low electron temperature indicates that the DRIBM may be responsible for the increase in transport with radius observed in HSX plasma edge region. Moreover, the magnitude of the particle diffusivity is estimated to be in the range of experimentally measured particle diffusivity at the edge of the HSX stellarator plasma.

Acknowledgments

This research was supported by the U.S. DoE under Grants Nos. DE-FG02-99E54546, DE-FG02-86ER53218 and DE-FG02-92ER54141.

---

[1] G. Bateman and D. Nelson, *Phys. Rev. Lett.* **41,** 1805 (1978).

[2] B. A. Carreras, P. H. Diamond, M. Murakami, J. L. Dunlap, J. D. Bell, H. R. Hicks, J. A. Holmes, C. E. Thomas, and R. M. Weiland, *Phys. Rev. Lett.* **50,** 503 (1983) and references therein.

[3] J. R. Myra, D. A. D'Ippolito, X. Q. Xu, and R. H. Cohen, *Phys. Plasmas* **7,** 4622 (2000).

[4] J. Weiland, *Collective Modes in Inhomogeneous Plasma*, (IOP Publishing LTD Bristol; Philadelphia 2000).

[5] A. Zeiler, J. F. Drake and B. Rogers, *Phys. Plasmas* **4,** 2134 (1992).

[6] R. G. Kleva and P. N. Guzdar, *Phys. Plasmas* **6,** 116 (1999).

[7] J. W. Connor and R. J. Hastie, *Phys. Plasmas* **6,** 4620 (1999).

[8] R. H. Hastie, J. J. Ramos and F. Porcelli, *Phys. Plasmas* **10,** 4405 (2003).

[9] P. N. Guzdar, J. F. Drake, D. McCarthy, A. B. Hassam and C. S. Liu, *Phys. Fluids B* **5,** 3712 (1993).

[10] B. N. Rogers and J. F. Drake, *Phys. Plasmas* **6,** 2797 (1999).

[11] X. Q. Xu, R. H. Cohen, T. D. Rognlien, and J. R. Myra, *Phys. Plasmas* **7,** 1951 (2000).

[12] A. H. Glasser, J. M. Greene and J. L. Johnson, *Phys. of Fluids* **18,** 875 (1975).

[13] X. Llobet, H. L. Berk and M. N Rosenbluth, *Phys. of Fluids* **30,** 2750 (1987).

[14] D. Correa-Restrepo, *Z. Naturforsch. A* **37,** 848 (1982).

[15] H. R. Strauss, L. E. Sugiyama, G. Y. Fu, W. Park and J. Breslau, *Nucl. Fusion* **44,** 1008 (2004).

[16] R. Kaiser *Nucl. Fusion* **33,** 1281 (1993).

[17] F. S. B. Anderson, A. F. Almagri, D. T. Anderson, P. G. Mathews, J. N. Talmadge, and J. L. Shohet, *Fusion Technology* **27**, 273 (1995).

[18] S. P. Gerhardt, J. N. Talmadge, J. M. Canik, and D. T. Anderson, *Phys. Plasmas* **12,** 056116 (2005)

[19] T. Rafiq and C. C. Hegna, *Phys. Plasmas* **13,** 062501 (2006).

[20] S. I. Braginskii, *Reviews of Plasma Physics* (Consultants Bureau, Newyork 1965) Vol. 1, p.205.

[21] J. W. Connor and R. J. Hastie, *Plasmas Phys. Control. Fusion* **27,** 621 (1985).

[22] J. W. Connor, R. J. Hastie, and J. B. Taylor, *Phys. Rev. Lett.* **40,** 396 (1977).

[23] C. C. Hegna and S. R. Hudson, *Phys. Rev. Lett.* **87,** 035001 (2001).

[24] M. Persson, J. L. V. Lewandowski and H. Nordman, *Phys. Plasmas* **3**, 3720 (1996).

[25] T. Rafiq, J. Anderson, M. Nadeem and M. Persson, *Plasmas Phys. Control. Fusion* **43**, 1363 (2001).

[26] S. P. Hirshman and O. Betancourt, *J. Comput. Phys.* **96**, 99 (1991).

[27] A. H. Boozer, *Phys. Fluids* **25**, 520 (1982).

[28] T. Rafiq and C. C. Hegna, *Phys.Plasmas* **12,** 112505 (2005).

[29] W. D. D'haeseleer, W. N. G. Hitchon, J. D. Callen, and J. L. Shohet, *Flux Coordinates and Magnetic Field Structure* (Springer-Verlag, Berlin; New York, 1991), Chapt. 6.

[30] D. T. Anderson, A. Abdou, A. F. Almagri, F. S. B. Anderson, J. M. Canik, W. Guttenfelder, C. Lechte, K. M. Likin, H. Lu, S. Oh, P. H. Probert, J. Radder, V. Sakaguchi, J. Schmitt, J. N. Talmadge, K. Zhai, D. L. Brower and C. Deng, *Fusion Science and Technology* **50,** 171 (2006).

[31] J. Weiland and A. Hirose, *Nucl. Fusion* **32,** 151 (1992).

Figure Captions:

Figure 1:(Color online) (a) The ballooning mode eigenfunction is shown as a function of θ (left panel) and the variation of normalized growth rate is shown as a function of ballooning parameter α (right panel) for $\theta_k = 0$, $\hat{s} = 0.1$, $k_\theta \rho_s = 0.3$, $\hat{\nu_e} = 0.023$, and $\beta = 0.0002$. (b) The ballooning mode eigenfunction is plotted as a function of θ for $\alpha = 0.2$ in the left panel and $\alpha = 1.0$ in the right panel.

Figure 2:(Color online) (a) Growth rate (left panel) and real part of the frequency (right panel) of the ballooning mode as a function of α for the RIMHD model (solid line) and the model with drift effects (DRIBM with $\triangle$ symbols) for $\hat{s} = -0.03$ and $k_\theta \rho_s = 0.1$. The other parameters are the same as those used in Fig.1. (b) Ballooning mode eigenfunction (right panel) as a function of θ for $\alpha = 0.05$ (left panel), and $\alpha = 0.2$ and $\alpha = 0.4$.

Figure 3:(Color online) (a) Growth rate (left panel) and real frequency (right panel) for the DRIBM mode as a function of $\hat{s}$ for $q = 1.0$, $k_\theta \rho = 0.1$ $\alpha = 0.10$, $\tau = 1.0$, $\beta = 0.002$, $\epsilon_n = 0.07$, $\theta_k = 0$, and (b) DRIBM eigenfunction as a function of θ for positive and negative values of shear.

Figure 4:(Color online) (a) Growth rate (left panel) and real frequency (right panel) for RIMHD modes (solid line) and the DRIBM ($\triangle$ symbols) modes, and as a function of $k_\theta \rho_s$ for $\hat{s} = -0.03$. The other parameters are the same as those used in Fig. 2.

Figure 5:(Color online) (a) Growth rate (left panel) and real frequency (right panel) for the drift-resistive-inertial ballooning mode (DRIBM) as a function of ϵ_n for $k_\theta \rho_s = 0.1$, $\alpha = 2q^2\beta/\epsilon_n$. The other parameters are the same as those used in Fig. 2. (b) Eigenfunction of the DRIBM is plotted for $\epsilon_n = 0.02$ and $\epsilon_n = 0.07$.

Figure 6:(Color online) (a) Growth rate (left panel) and real frequency (right panel) for the DRIBM as a function of β for $\epsilon_n = 0.07$, $\alpha = 2q^2\beta/\epsilon_n$, $q = 1.0$, $k_\theta \rho_s = 0.01$ and $\tau = 0.25$. (b) The ballooning mode eigenfunction is plotted as a function of θ for four values of β.

Figure 7:(Color online) (a) Growth rate (left panel) and real frequency (right panel) for the DRIBM as a function of β for $k_\theta \rho_s = 0.2$ and $\tau = 4.0$. The other parameters are the

same as those used in Fig. 6. (b) The ballooning mode eigenfunction is plotted as a function of θ for $\beta = 0.006$ and $\beta = 0.012$.

Figure 8:(Color online) Growth rate (left panel) for the highly resistive (HR) and resistive-inertial MHD ballooning modes (RIMHD) in the electrostatic limit as a function of $(k_\perp \rho)^2$ in QHS configuration for $s = 0.8980$, $\tau = 1$, $R\nu_{ei}/2c_s = 0.42$, $\theta_k = 0.0$, $\epsilon_n = 0.07$ and $\theta_0 = 0$, $\zeta_0 = 0$ field line. Ballooning mode eigenfunctions as a function of θ for $(k_\perp \rho)^2 = 0.24$ (right panel) and for $(k_\perp \rho)^2 = 0.6$ in Fig.9a

Figure 9:(Color online) Growth rate (left panel) for the resistive-inertial MHD ballooning modes (RIMHD) in the electrostatic limit as a function of $(k_\perp \rho)^2$ for QHS and Mirror cases. The other parameters are the same as those used in the Fig. 7. (b) Ballooning mode eigenfunctions as a function of θ for $(k_\perp \rho)^2 = 0.02$ (right panel).

Figure 10:(Color online) The effective particle diffusivity D_n plotted against the normalized density gradient, g_{ni} for full model (the solid curve), ignoring electron inertia from the full model (the curve denoted with dashes) and ignoring the parallel ion dynamics (the dashed curve) from the full model for $n = 10^{18}\,\mathrm{m}^{-3}$, $\mu_\perp = 0.0$, $B = 0.5\,\mathrm{T}$, $\bar{a} = 0.12\,\mathrm{m}$, $\bar{R} = 1.2\,\mathrm{m}$, $q = 1.0$, $\hat{s} = 0.03$, $Z_{eff} = 1.5$, $\nabla \mathrm{T}_i = g_{Ti} = 0.0$ and $k_\perp \rho_s = 0.1$.

Figure 11:(Color online) The effective particle diffusivity D_n plotted against the normalized density gradient, g_{ni} for full model for $T_e = 10\,\mathrm{eV}$, $20\,\mathrm{eV}$, $30\,\mathrm{eV}$, $40\,\mathrm{eV}$ and $T_i = 10\,\mathrm{eV}$. The other parameters are the same as those used in Fig. 10.

Figure 12:(Color online) The effective particle diffusivity D_n plotted against the electron ion collision frequency, ν_{ei}, for full model for $T_e = 20\,\mathrm{eV}$, and $T_i = 10\,\mathrm{eV}$. The other parameters are the same as those used in Fig. 10.

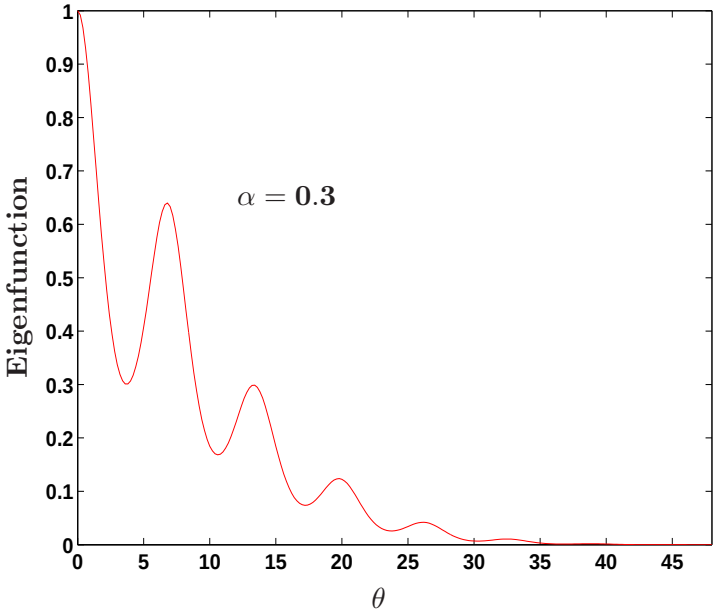

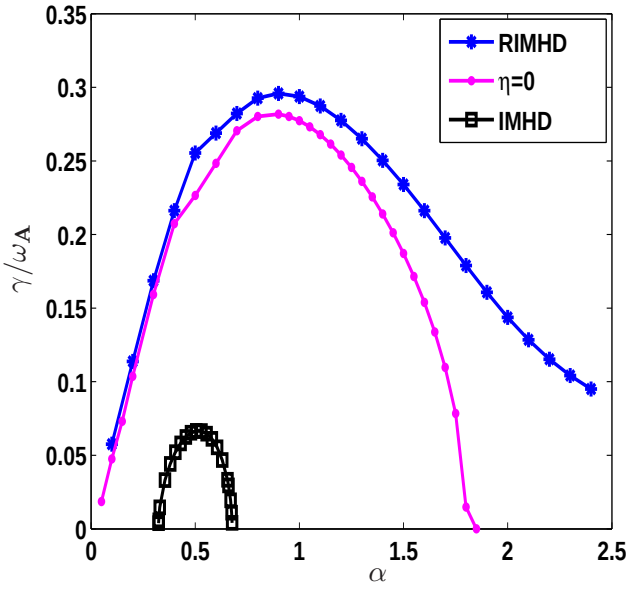

Figure 1a

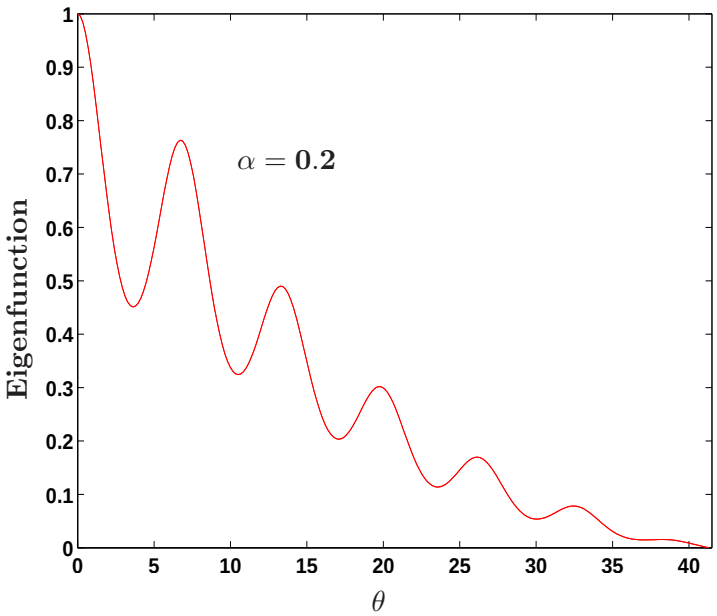

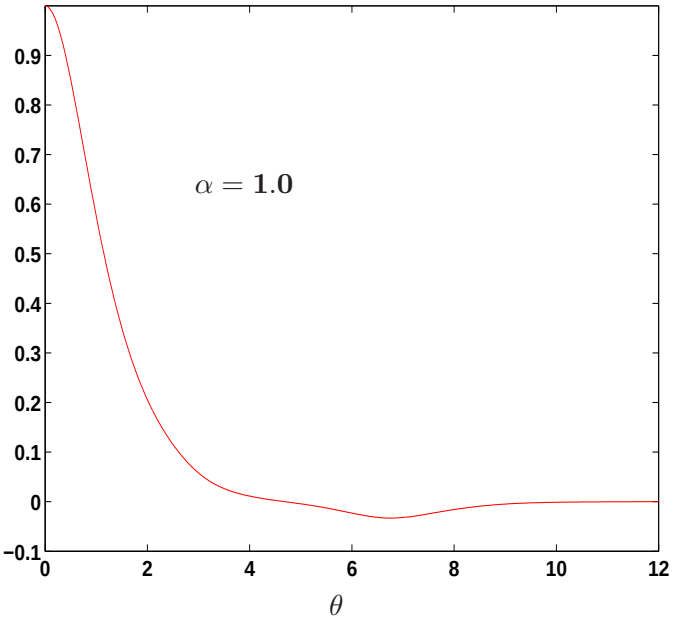

Figure 1b

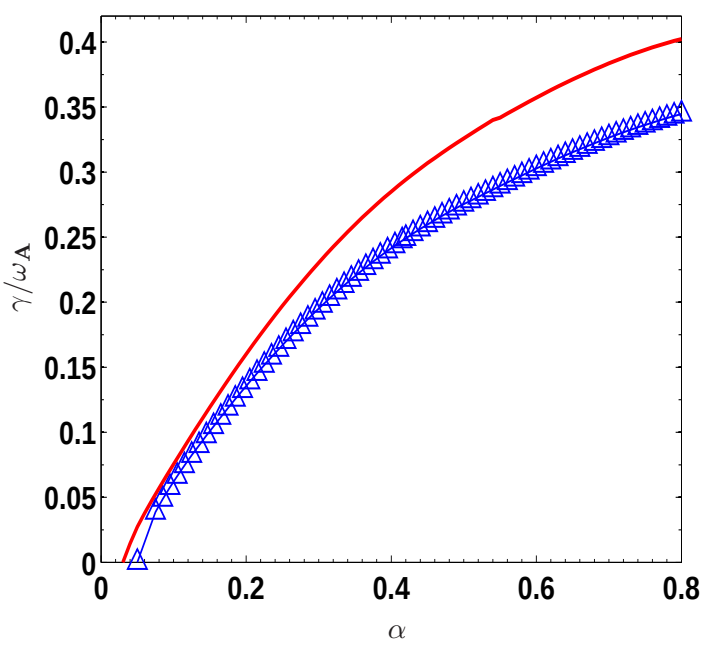

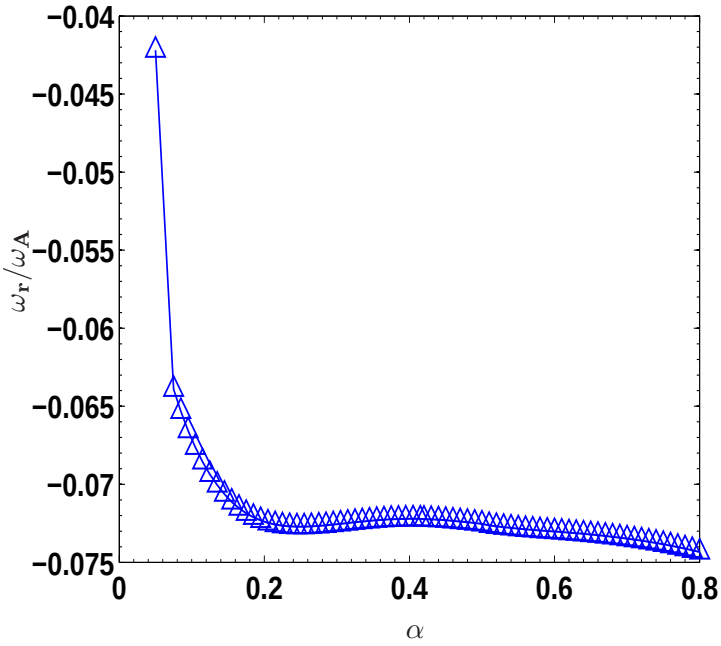

Figure 2a

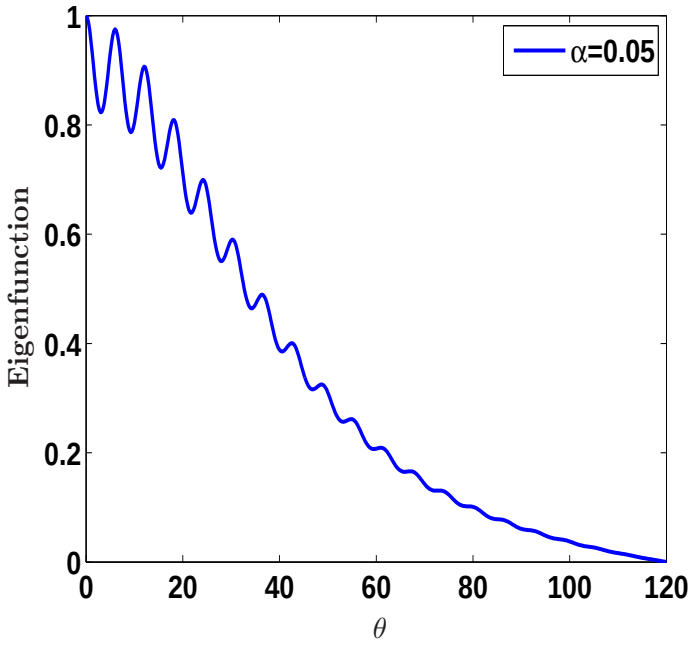

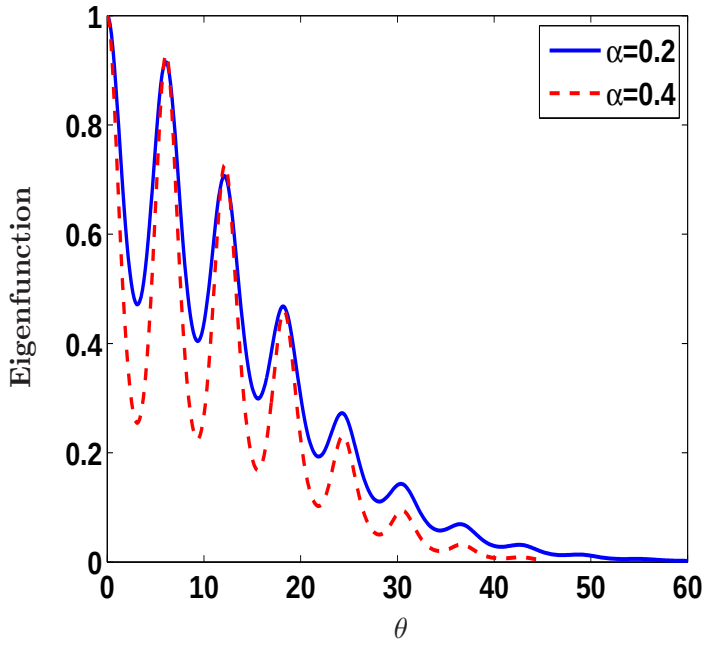

Figure 2b

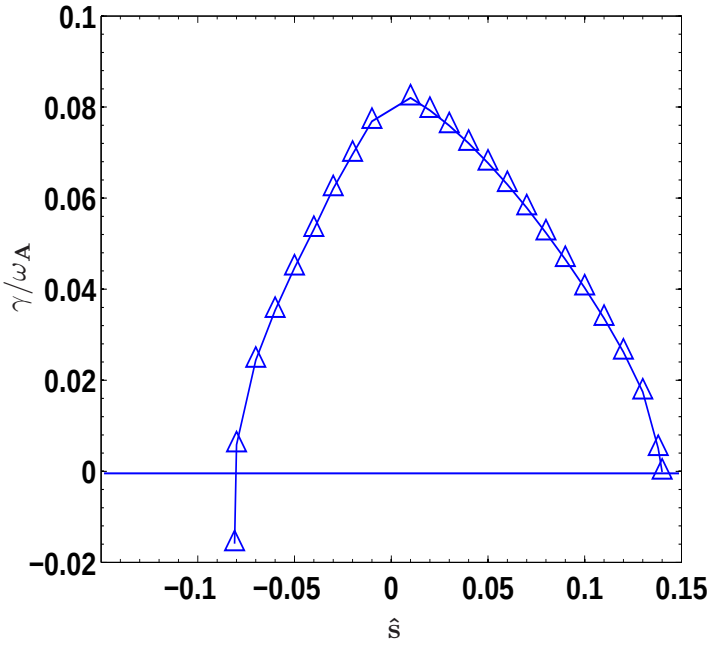

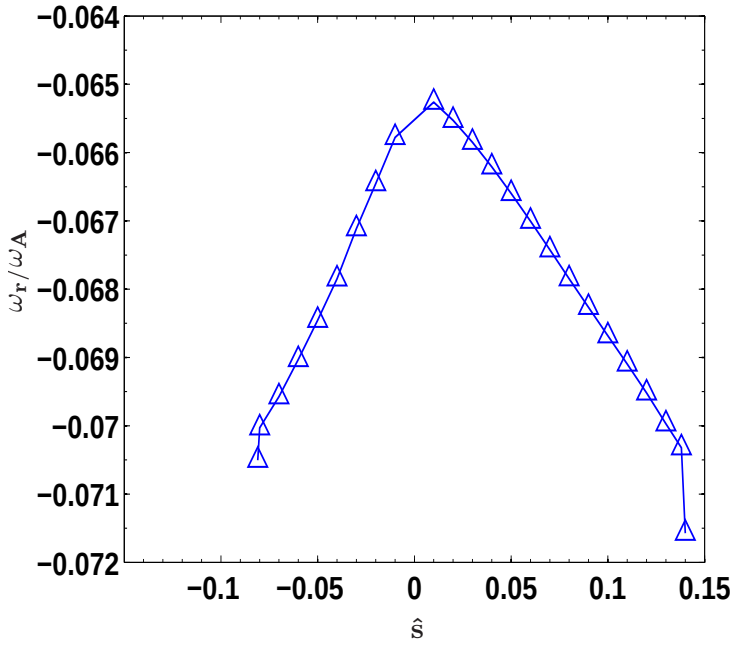

Figure 3a

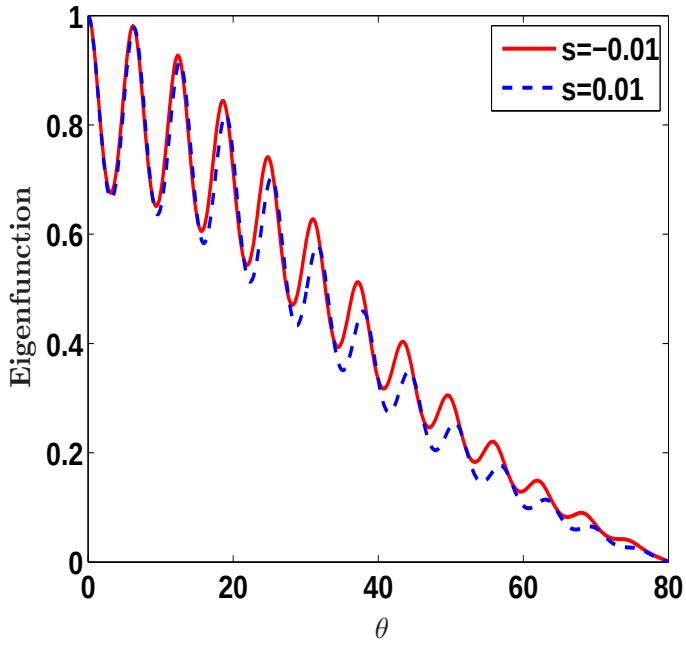

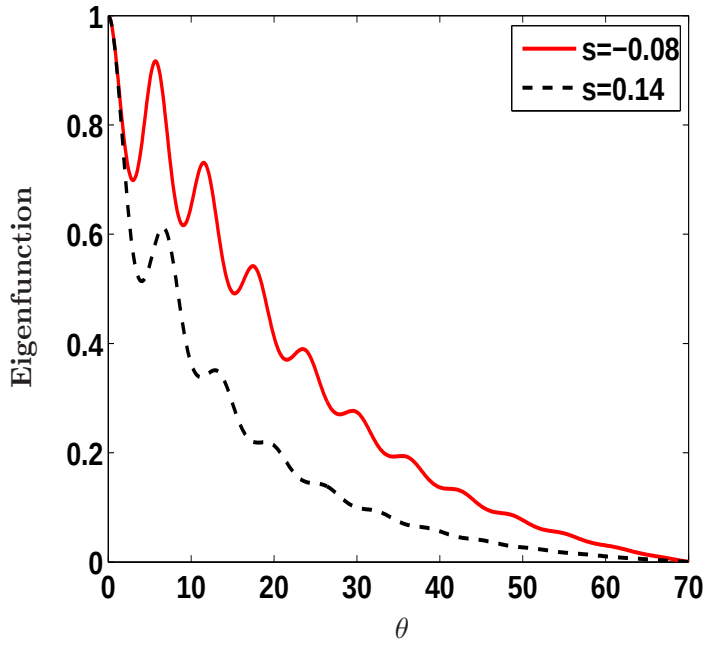

Figure 3b

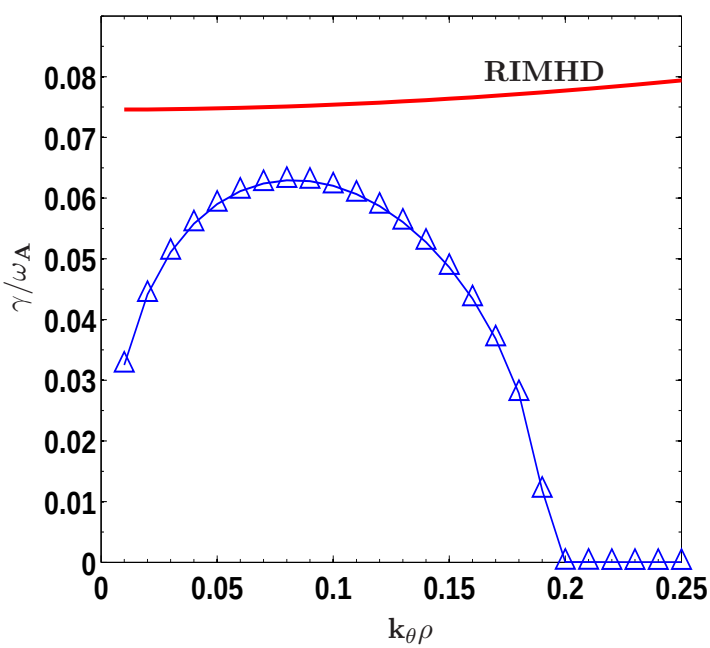
RIMHD
0.08
0.07
0.06
0.05
0.04
0.03
0.02
0.01
0
0
0.05
0.1
0.15
0.2
0.25
γ/ω_A
$k_\theta\rho$

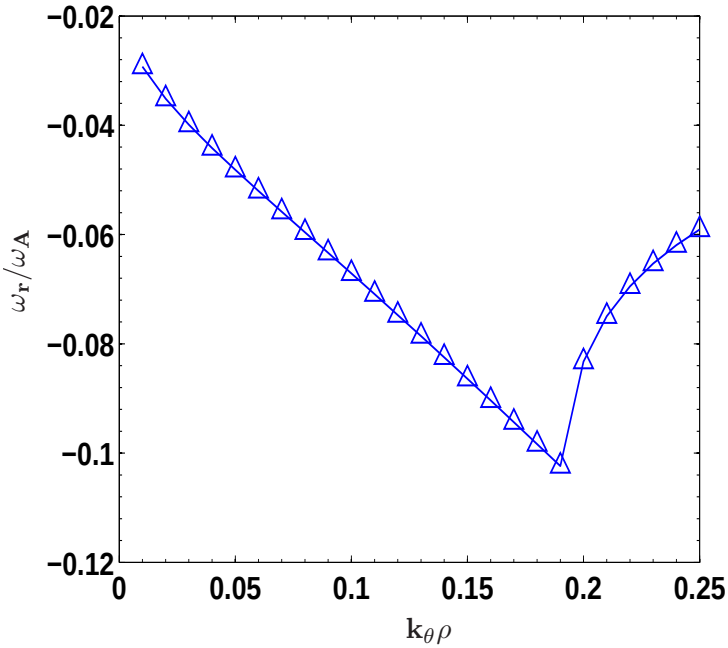
−0.02
−0.04
−0.06
−0.08
−0.1
−0.12
0
0.05
0.1
0.15
0.2
0.25
ω_r/ω_A
$k_\theta\rho$

Figure 4

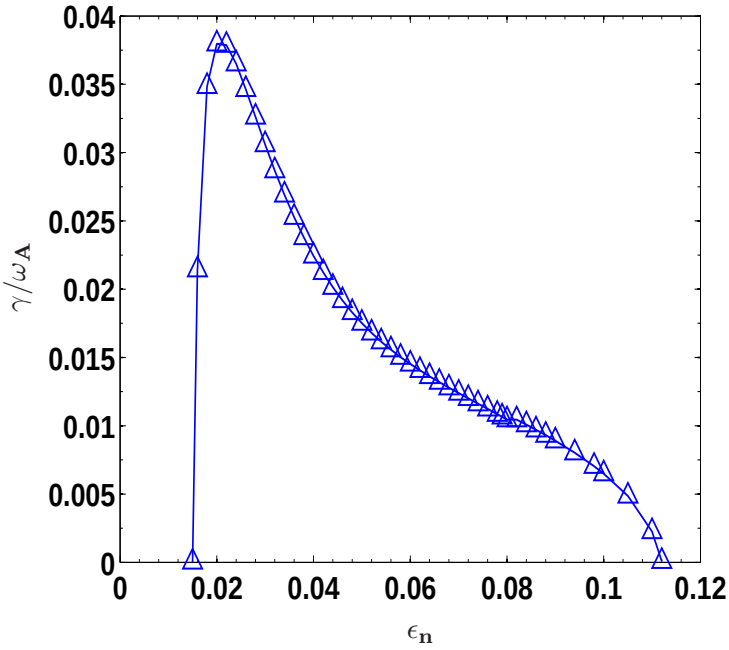

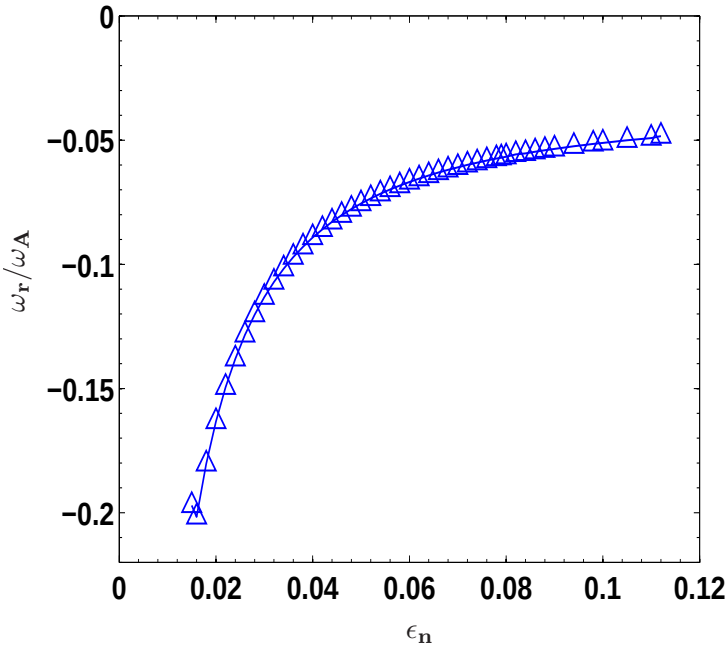

Figure 5a

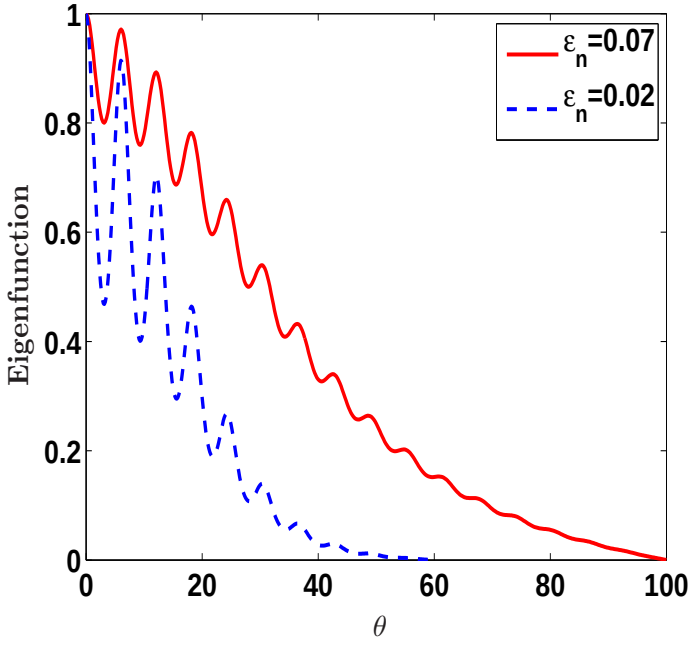

Figure 5b

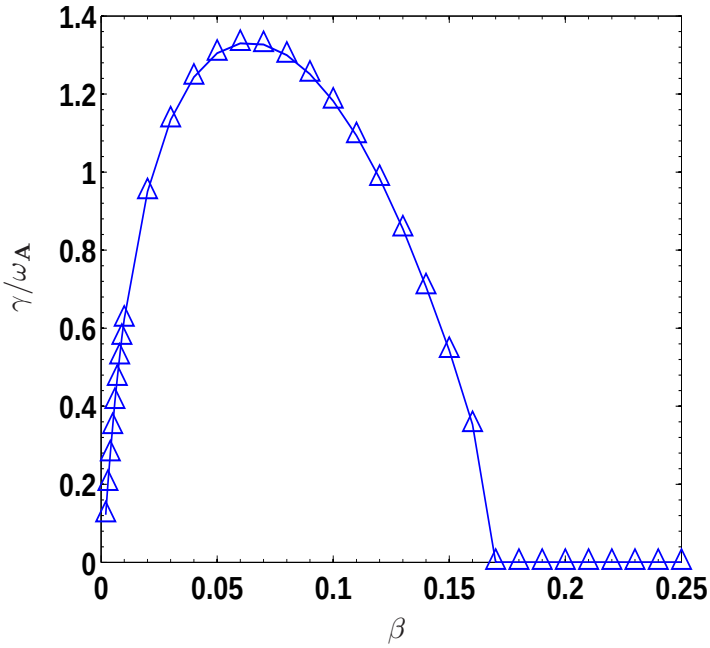

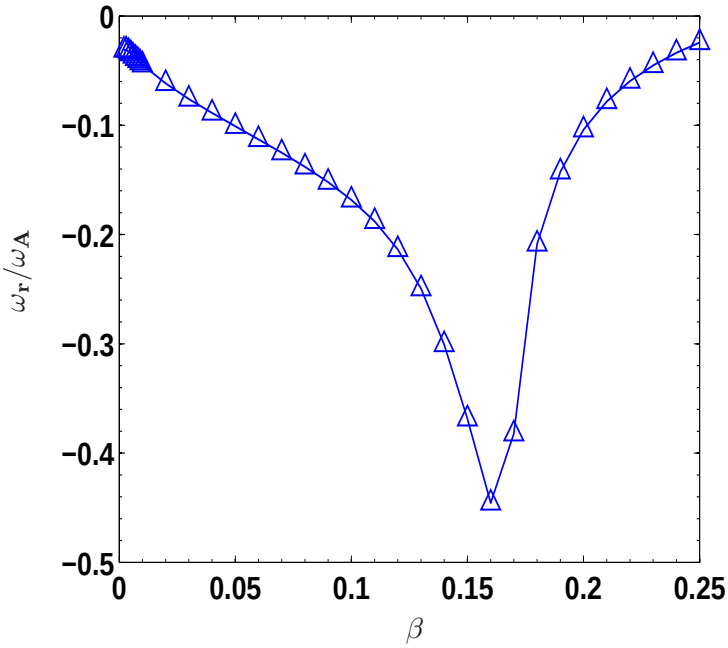

Figure 6a

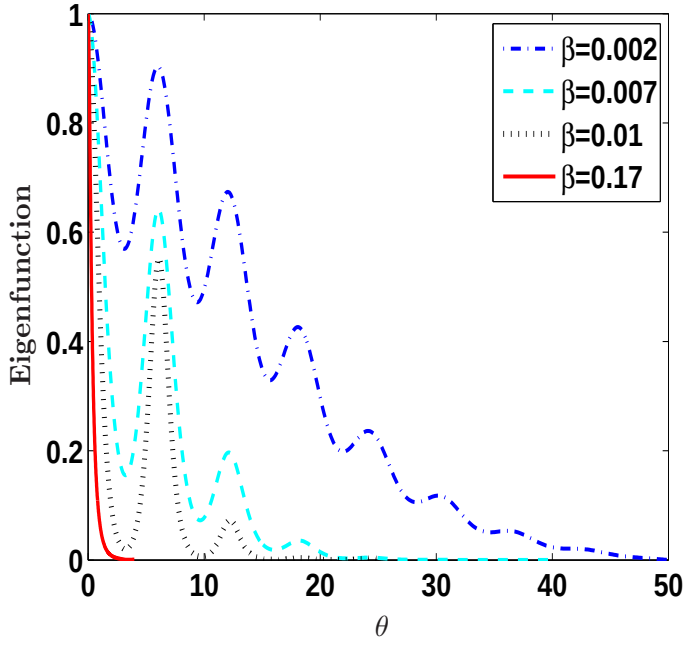

Figure 6b

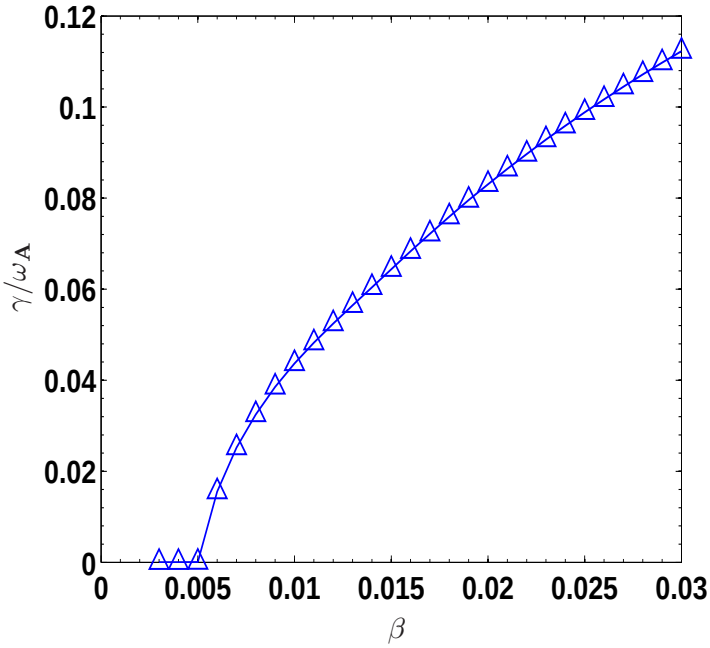

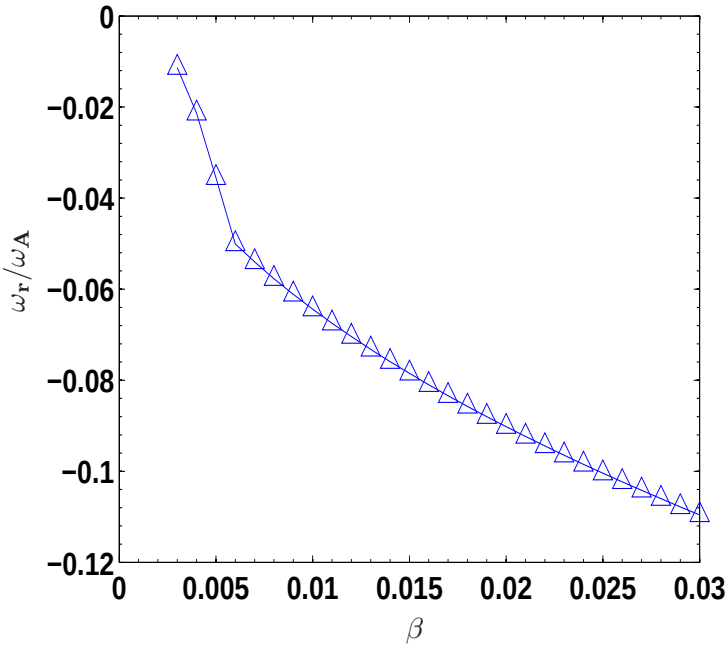

Figure 7a

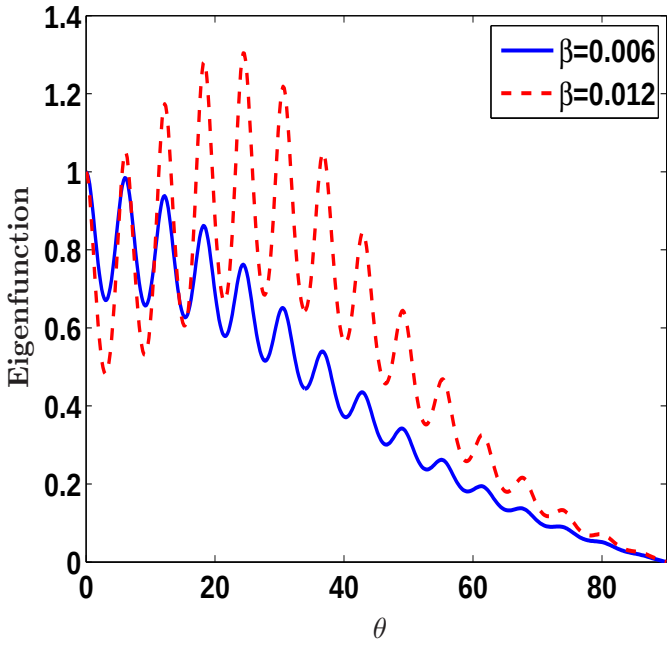

Figure 7b

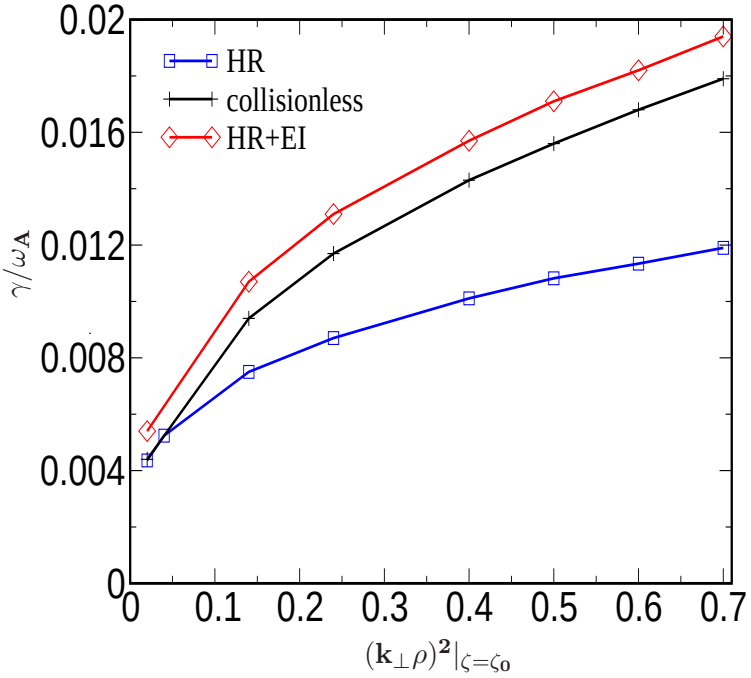
0.02
0.016
0.012
0.008
0.004
0
0
0.1
0.2
0.3
0.4
0.5
0.6
0.7
HR
collisionless
HR+EI
γ/ω_A
$(\mathbf{k}_\perp\rho)^2|_{\zeta=\zeta_0}$

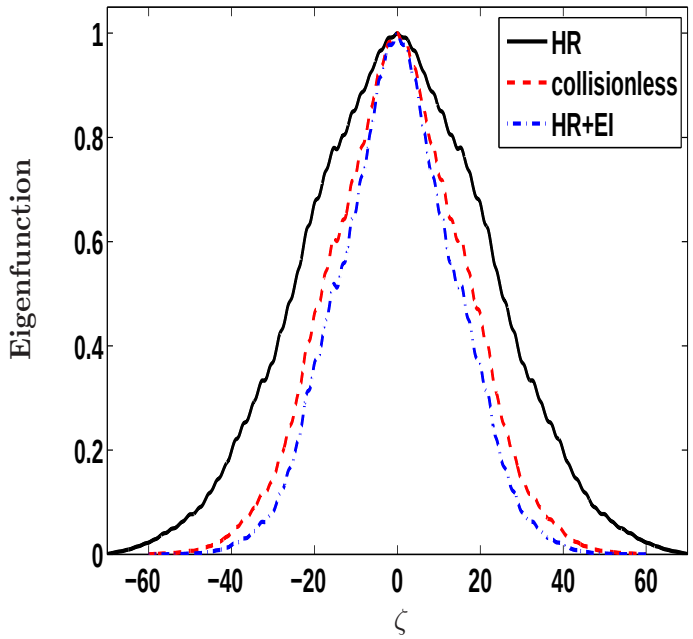
1
0.8
0.6
0.4
0.2
0
−60
−40
−20
0
20
40
60
HR
collisionless
HR+EI
Eigenfunction
ζ

Figure 8

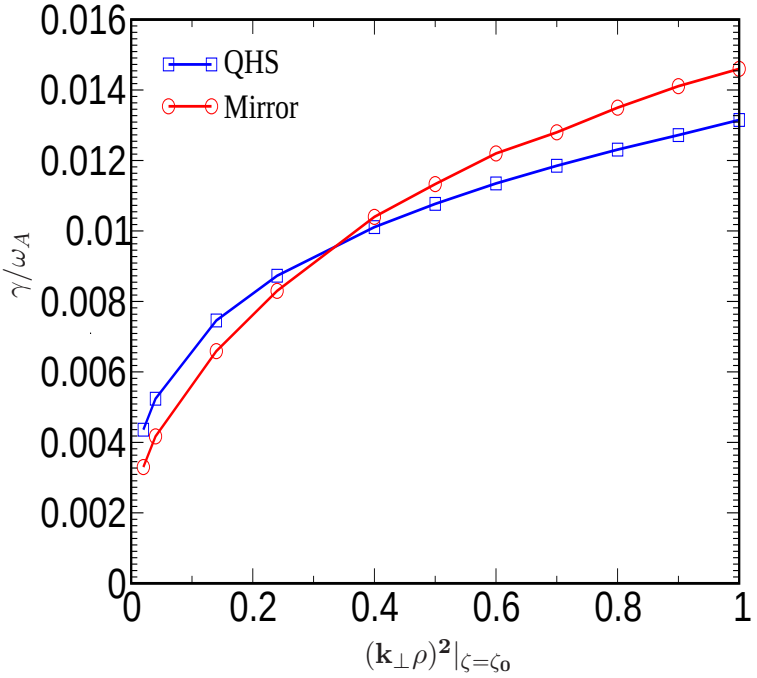

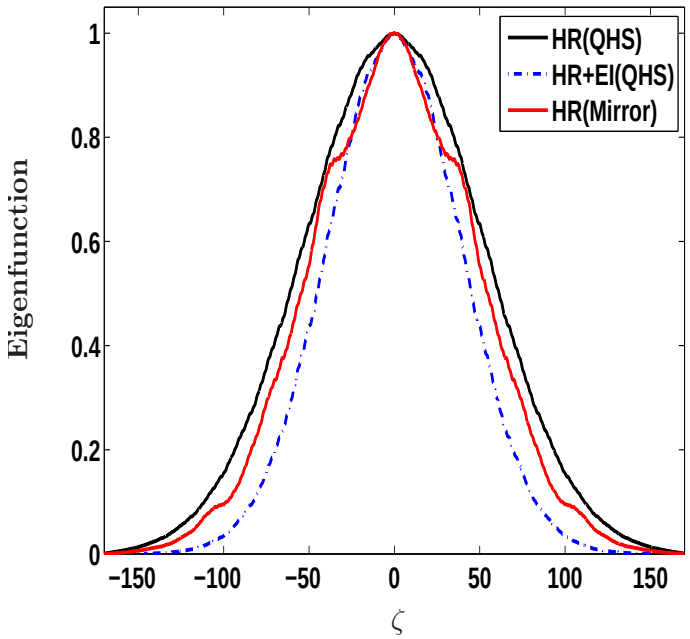

Figure 9

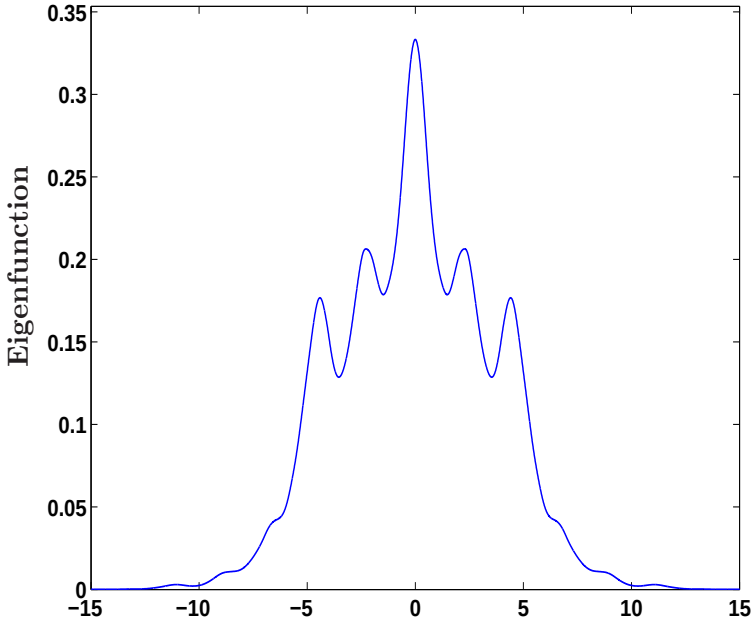

Figure 9a

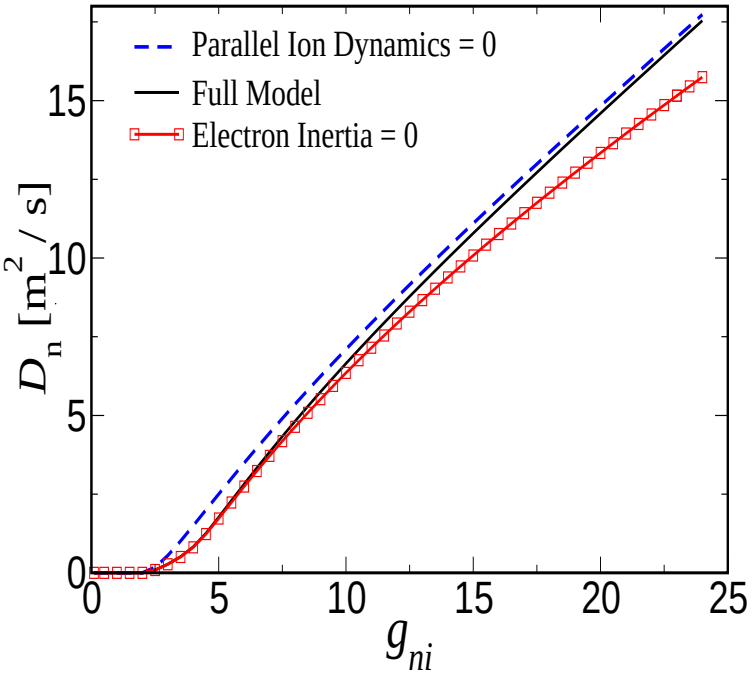
Parallel Ion Dynamics = 0
Full Model
Electron Inertia = 0
D_n [m^2 / s]
g_{ni}
0
5
10
15
20
25

Figure 10

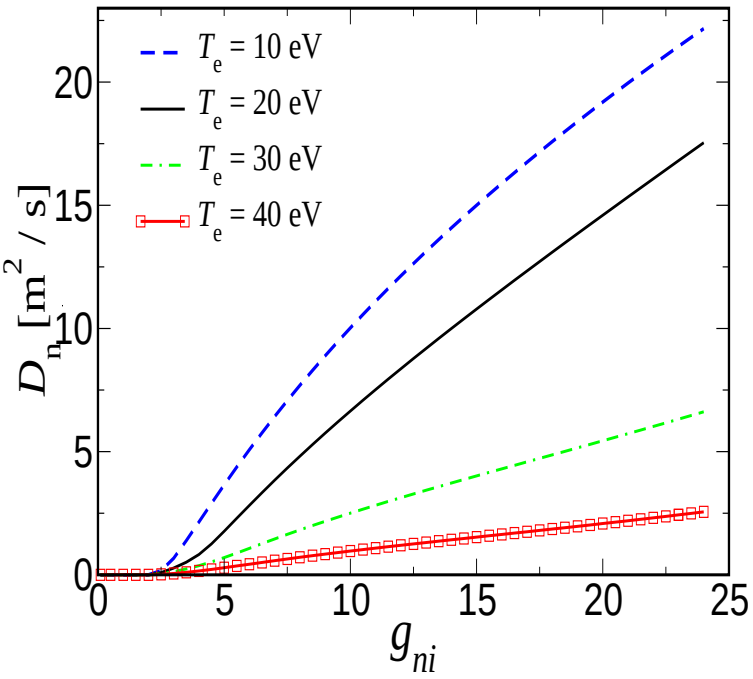

Figure 11

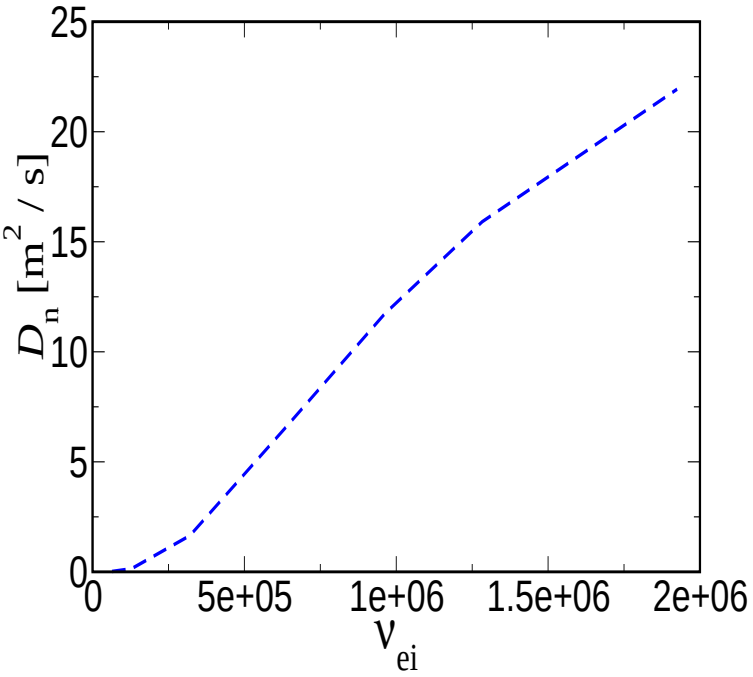

Figure 12